Delft University of Technology

Hermes - Wind Energy Harvesting Wireless System for Sensing AoA and Wind Speed

Sharma, Suryansh; Simha, Ashutosh; Venkatesha Prasad, Rangarao; Gokhale, Vineet; Narayana, Sujay

Important note
To cite this publication, please use the final published version (if applicable).
Please check the document version above.

Hermes - Wind Energy Harvesting Wireless System for Sensing Angle of Attack and Wind Speed

Suryansh Sharma, Ashutosh Simha, R. Venkatesha Prasad, Vineet Gokhale and Sujay Narayana

Abstract—In this paper, we present *Hermes* – a novel, low-cost, wireless, batteryless, energy harvesting system for aerial vehicles for sensing wind speed and Angle of Attack (AoA) concurrently. Hermes comprises a set of piezoelectric films which flutter due to incoming wind and the characteristics of this *aeroelastic flutter* are utilized for determining the wind speed and AoA of the head-wind. Note that in our work we restrict the notion of flutter to high frequency oscillations due to incoming air flow. Hermes consists of five piezoelectric flags that are mounted on rigid clamps specifically placed at different angles. We designed Hermes to maximize the sensing performance and energy harvesting capability simultaneously, without compromising either accuracy or harvesting efficiency. Our current prototype can harvest the power of $440\,\mu W$ on average. Over a wide range AoA from -10° to 30°, the estimation of the wind speed is within 0.7 km/h error with 90% probability, and AoA error is within 1.2° with 90% probability. Since Hermes necessitates no wires and batteries and is a low-cost sensor, it is well suited for a range of UAVs, gliders, and aircraft, which require flexible sensor placement and do not require new wiring, which is often complex in aircraft. Hermes is the first of its kind that exploits piezoelectric energy harvesting to simultaneously sense AoA and wind speed. This work is expected to open up new avenues for interdisciplinary research on embedded computing devices for aerospace applications.

Index Terms—Aerial Systems: Applications; Embedded Systems for Robotic and Automation; Sensor Networks

I. INTRODUCTION

ANGLE OF ATTACK(AoA) is a fundamental aerodynamic parameter defined as the angle between the reference line of an airborne body (which is traditionally the chord line of an airfoil in the 2D aerodynamic setup) and the relative wind velocity vector, as shown in Fig. 1a. Accurate measurement of AoA along with the wind speed is crucial for maintaining appropriate lift and preventing stall regimes during take-off, landing, and cruise [1]. Sensors for measuring these parameters have played an instrumental role in realizing the human desire to fly, starting from the advent of the first human aircraft in 1903 [2]. Although these sensors have been integral elements of an aircraft for over a century [3], they are prone to inaccuracies and faulty measurements even today [4]–[6]. As a consequence of the criticality of these parameters, an aircraft needs redundant (fail-safe) AoA and wind speed sensors for improving accuracy and reliability.

While the accurate measurement of AoA and wind speed is itself non-trivial, there are several constraints and restrictions,
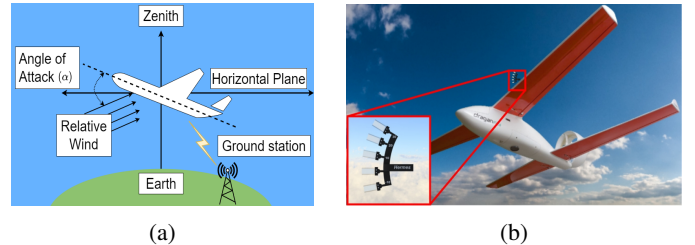
Fig. 1: (a) Angle of Attack (AoA) made by an aircraft. (b) Conceptual view of Hermes on a fixed-wing UAV.

especially for small-scale fixed-wing aircraft, autonomous gliders and UAVs, which make the problem of sensor design even more challenging due to the following reasons. ❶ Deploying multiple standard sensors such as the ones based on pitot tube [7], [8] are expensive which makes them infeasible for the above-mentioned applications. ❷ To meet the low energy budget and to add resilience, it is best if redundant sensors are self-powered, which is not enabled by existing solutions [9], [10]. ❸ In any aircraft, new wiring may require a huge amount of planning and effort. To avoid inherent problems with wires, communication with the sensors may need to be carried out wirelessly. ❹ The sensor should be lightweight and have a small form-factor for convenient mounting and retrofitting to any aircraft. ❺ Separate sensors for AoA and wind speed measurements increase the bulk of the measuring unit. On the other hand, measuring one of the quantities and inferring the other (if feasible) leads to inaccuracies. A sensor for simultaneously measuring the two quantities is necessary. While pitot tubes are the primary sensors for aviation, Hermes is not necessarily meant to replace them but complement them by providing an additional, self powered sensing modality, increasing redundancy and thereby reliability. Although the literature provides a few works that have addressed some of these challenges [11]–[14], a comprehensive solution that addresses all the above challenges is non-existent. This severe limitation in the state of the art inspires us to come up with a novel sensor design. The question we address in this paper is: **Is there a simple, holistic solution that addresses all of the aforementioned challenges?**

To address the above challenges, we developed *Hermes*[1], which is a wind-powered, wireless sensor for low-cost, reliable, and robust measurement of AoA and wind speed. Fig. 1b depicts a conceptual view of the proposed system mounted on an aircraft. A first of its kind sensor, Hermes leverages as a source of energy the very physical phenomenon that it is designed to measure – the wind speed. Hermes employs piezoelectric films to utilize *flutter*, – a destructive

[1]Named after the ancient Greek god of travelers.
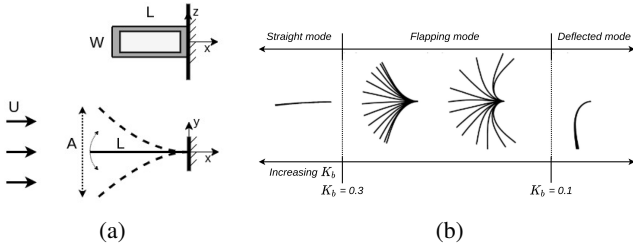
Fig. 2: (a) Inverted flag geometry of an elastic sheet. The solid (horizontal) line in the left image shows the sheet, and the dashed lines indicate curvature. The image on right shows the sheet dimensions. (b) Illustration of the three modes

phenomenon that is inevitably introduced by the wind – to accurately sense AoA and wind speed as well as efficiently harvest energy entirely avoiding the use of batteries. Our primary contributions are summarized here:

1) We conduct extensive wind tunnel experiments to optimize sensing and energy harvesting performance simultaneously.
2) In order to address the highly nonlinear sensor characteristics we devise *Nonlinear Surface Regression* (NSR) – a data-driven algorithm for accurate estimation.
3) We show that in addition to accurate sensing the energy harvesting capability of Hermes is sufficient for powering wireless transmission, thereby enabling batteryless operation.

II. THEORETICAL BACKGROUND

A. Aeroelastic flutter: A destructive ally

An elastic plate subjected to axial fluid flow begins to flutter above the critical velocity of the fluid, where the destabilizing forces overpower the stabilizing effect of the rigidity of the structure [15]. Though considered a *destructive* phenomenon [16], we leverage flutter to harvest energy from the fluid momentum via the piezoelectric effect.

B. Inverted Flags and their dynamics

The immersed structure for this work consists of thin elastic piezoelectric PVDF (Polyvinylidene fluoride) films, which are placed in the wind flow. This allows for two distinct potential configurations: a *regular flag* and an *inverted flag*. An inverted flag is the mirror image of a regular flag with the leading edge left free to move, and the trailing edge is fixed. Fig. 2a shows the schematic of the inverted flag geometry for an elastic sheet. The sheet is shown using a solid straight line, and the curved dashed lines indicate the curvature of the film. A denotes the maximum displacement between the tips in the y-axis, while L and W denote the length and width of the sheet, respectively.

The inverted flag configuration for inducing flutter was first proposed by [17] and is motivated by the fact that any mechanical model with a free front and fixed rear end will be, in general, more susceptible to instability when faced with external axial loading than a regular flag. To explain, we can give a simple analogy of leaves fluttering in the breeze irrespective of their orientation to the wind, which justifies using this configuration as an alternative to the regular flag for flow-induced flapping.
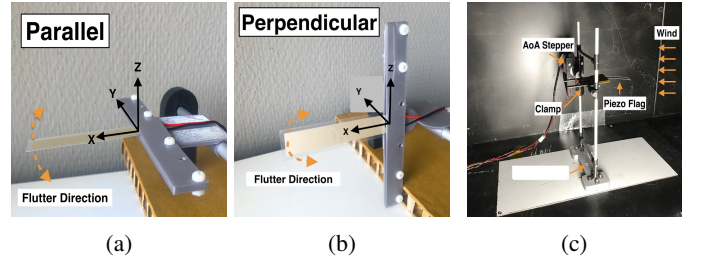
Fig. 3: (a) Parallel (in-plane) configuration of inverted flag. (b) Perpendicular (out of plane) configuration of inverted flag. (c) Constructed test rig.

There are three important parameters which are used to characterize the dynamics of interaction between fluid flow and an inverted elastic film: mass ratio μ, aspect ratio A_R, and bending stiffness K_b [18]–[20]. They are calculated as,

$$\mu = \frac{\rho_s h}{\rho_f L} \tag{1}$$

$$A_R = \frac{W}{L} \tag{2}$$

$$K_b = \frac{E h^3}{12 \rho_f U^2 L^3 (1 - \nu^2)} \tag{3}$$

Here ρ_s is the elastic sheet density, ρ_f is the fluid density, h is the thickness of the film, U is the free-stream velocity, E is Young's modulus, ν is the Poisson's ratio. μ represents the relative magnitude of structure to fluid inertial forces, while K_b characterizes the relative magnitude of bending forces to the fluid inertial forces and can be used to classify three dynamical regime or modes:

Straight mode ($K_b \geq 0.3$): In this mode, the sheet remains straight. This regime exhibits behaviour analogous to fixed-point stability where after an initial disturbance, the sheet experiences positive damping and returns to a stretched-straight position.

Flapping mode ($0.1 < K_b < 0.3$): In this mode, the sheet will flap from side to side and the deflection will be periodic. The magnitude of oscillations is the maximum in this mode.

Deflected mode ($K_b \leq 0.1$): In this mode, the sheet bends in one direction and maintains a highly curved or deformed shape. The three modes are shown in Fig. 2b. The reasons for using inverted flags in Hermes are higher harvested energy, increased reliability, range and robustness [17], [17], [21], [22]

III. CONTROLLED WIND TUNNEL EXPERIMENTS

We now describe the various design aspects of Hermes using a controlled wind tunnel setup **(videos in [23])**. We begin by characterizing the voltage response of the inverted piezoelectric flag for optimizing the performance of sensing and energy harvesting. We study the effect of dimension and orientation of the flags on the harvested energy and sensing. Let α and U denote AoA and wind speed, respectively. The characterization is also used to develop an empirical model used for sensing.

A. Wind tunnel setup

All these experiments are performed in a low-speed open jet wind tunnel facility with a cross-section of $0.4\,\text{m} \times 0.4\,\text{m}$ that

TABLE I: Physical parameters of the piezoelectric flags.

Physical Quantity	Value		
	Small	Medium	Large
PVDF film	LDT1-028K/L	LDT2-028K/L	LDT4-028K/L
Length L (mm)	30	60	100
Width W (mm)	15	15	20
Thickness h (mm)	0.205	0.205	0.205
Aspect Ratio A_R	0.5	0.25	0.2
Mass Ratio μ	10	5	3
Capacitance (nF)	1.38	2.78	11.0
Young's Modulus E (GPa)	2.165	2.59	3.5
Film Density ρ_s (Kg/m^3)	1780	1780	1780
Poisson's Ratio ν	0.34	0.34	0.34

Fig. 4: Three flapping regimes for piezoelectric flag and corresponding voltage signals.

could produce U between 0 and 30 m/s. The wind speed was measured using an integrated pressure measurement system that used four-point pressure differential readings. The accuracy of the wind speed measurement in the setup is ± 0.10 m/s. In *parallel* configuration (Fig. 3a), the flutter is observed in the z plane, while in *perpendicular* configuration (Fig. 3b), it is in the $x - y$ plane. A specialized test rig (Fig. 3c) is made to accurately change the orientation of the flag to the incoming wind and effectively set AoA. The test rig is comprised of a wooden base with an aluminum structure created using 3D-printed holders and 7 mm aluminum rods. Two NEMA 17 stepper motors were used to orient the flags in the $x - y$ and the z direction, thereby setting the angle of sideslip and AoA, respectively.

The output of the piezoelectric flag was measured by recording the output voltage from a single PVDF membrane, by incrementally changing AoA from 0° up to 55° for each wind speed and for both flag orientations.

B. Design of piezoelectric flag

Different flag designs comprised of widely available, commercial off the shelf, single poled piezoelectric films from TE Connectivity [24] with a constant thickness $h = 205\,\mu$m. These PVDF membranes were typically laminated with a 125 μm polyester layer to a 28 μm or 52 μm piezoelectric film element. These laminated films provide an inherent structural rigidity when subjected to flow, thus enabling their direct use as inverted flags. Further, when the laminated films are used in deflected mode, they develop much higher voltage compared to non-laminated film elements. Additionally, the neutral axis of the film is in the laminate rather than in the film which results in the film getting strained more when flexed and causing less charge cancellation [24]. Three films were used to prepare three flags with properties (W, L, μ): *small* - (15 mm, 30 mm, 10), *medium* - (15 mm, 60 mm, 5), and *large* - (20 mm, 100 mm, 3).

IV. CHARACTERIZATION OF INVERTED FLAG

A. Identification of three flapping regimes

We observed the three regimes of flutter governed by the value of bending stiffness K_b. The flapping regimes and the generated voltage waveform for a medium-sized flag in the perpendicular configuration are shown in Fig. 4. We observed flutter for $K_b = 0.1$ to 0.3 [17], [22]. We did, however, observe asymmetrical oscillations for both the parallel and perpendicular. This can be attributed to the different styles of mounting
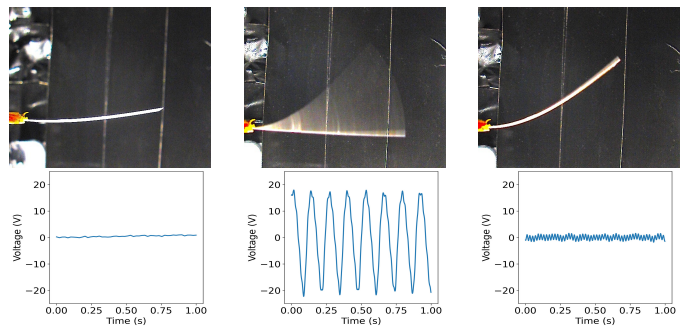
clamp we used compared to other similar experiments where the films were mounted on an aluminum rod [22].

B. Energy harvesting performance

The energy harvesting potential and energy density of different flags were characterized by observing the generated power. This was calculated by using the load resistance R_L and RMS value of the generated voltage. The peak voltage was found for every 100 samples and averaged over 1 s and then used to calculate the RMS voltage. Fig. 5 shows the effect of the mass ratio of the flags on the harvested power over varying wind speeds. All three flags experienced flutter over different wind speed ranges. It can be seen that for the small aspect ratio ($A_R < 1$), the small flag with $\mu = 10$ generates the largest power. The large flag had a smaller wind speed range and did not possess a very high power density for $A_R = 0.2$ and was thus found to be unsuitable for our sensor. The figure also shows the power densities for small and medium flags interpreting them in the context of K_b. Both flags show flutter between $K_b = [0.1, 0.3]$ with the maximum power density for the $K_b = 0.1$ case. Fig. 5 also shows that the wind speed range can be significantly modified by varying the geometric properties of the film. This is possible by manipulating the dimensions as well as the physical properties of the flags used, namely Young's modulus and Poisson's ratio. In this work, we have demonstrated the high potential of Hermes using only the commercially available COTS piezoelectric films. However, by customizing the design (such as a tapering or trapezoidal shape for instance), the sensing range can be significantly increased.

Since power density of the inverted flags is sensitive not only to the mass ratio but also to the aspect ratio of the flags, experiments were carried out with eight additional flags with varying dimensions as described in Section III. Fig. 6 shows the resulting power generated with varying aspect ratios for given wind speed and bending stiffness for flags for $\mu = 5$ and 10. The power generated increased considerably with the increase in aspect ratio owing in part to the additional PVDF films and partly due to increased flapping amplitude which can be inferred from the increased peak voltage. This result can also be verified in [22].

Finally, the range of AoA and wind speed for effective energy harvested can be discerned from Fig. 7. Clearly, the small flag shows a usable range of energy generation over the
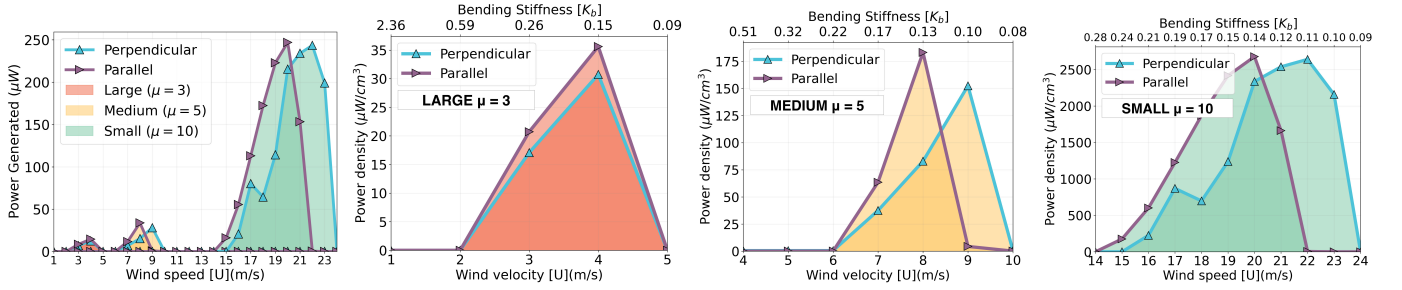
Fig. 5: Evaluation of harvested energy by all flags for $\alpha = 0$ (left) and interpreting the power density variations with bending stiffness for $\mu = 3$, $\mu = 5$ and $\mu = 10$.
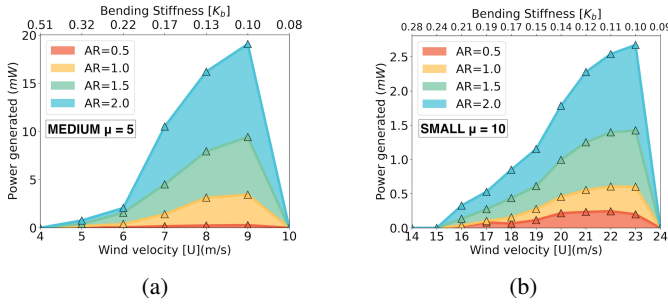
Fig. 6: Evaluation in energy harvested with varying A_R for (a) $\mu = 5$ and (b) $\mu = 10$ for different wind speeds with $\alpha = 0$.
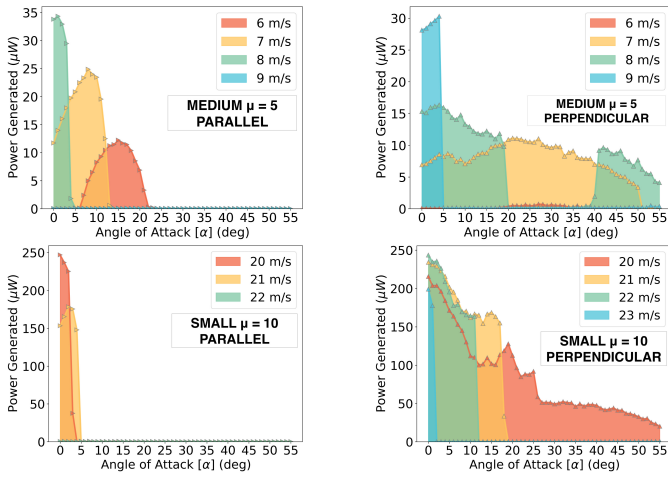
Fig. 7: Evaluation in harvested energy for different α and U, and flag orientations.

entire range of $\alpha \in [0, 55]$ for $K_b \in [0.1, 0.15]$, justifying our choice of the small flag in the perpendicular configuration.

C. Voltage features for sensing

Here, we analyzed the voltage generated by the piezoelectric flag for sensing wind speed and AoA in terms of (a) peak voltage (V_p) and (b) zero crossing frequency (f_z). V_p matches with the peak amplitude of flapping, while f_z relates to the flapping frequency. These two features thus represent the flutter characteristic in the electrical domain.

Figs. 8 and 9 show the trends observed for these two features for different α, U and flag orientations. The graphs are plotted for the mean value from 5 separate trials with a trial duration of 5 s. V_p is calculated over every 100 samples and averaged over
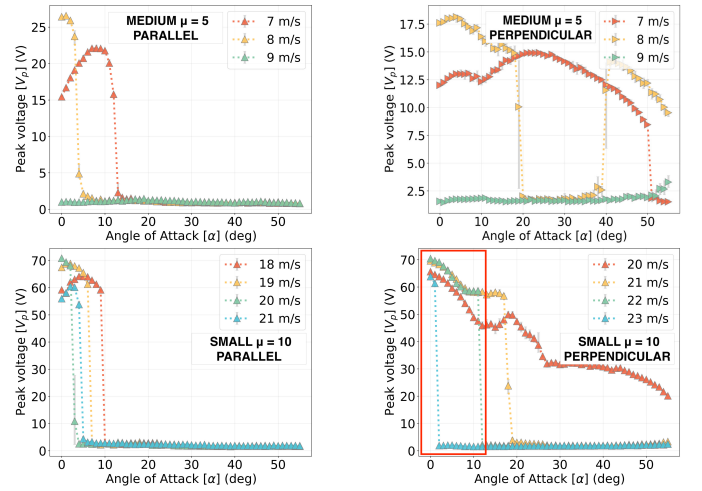
Fig. 8: Evaluation of peak voltage variation obtained for different α, U, and flag orientation.
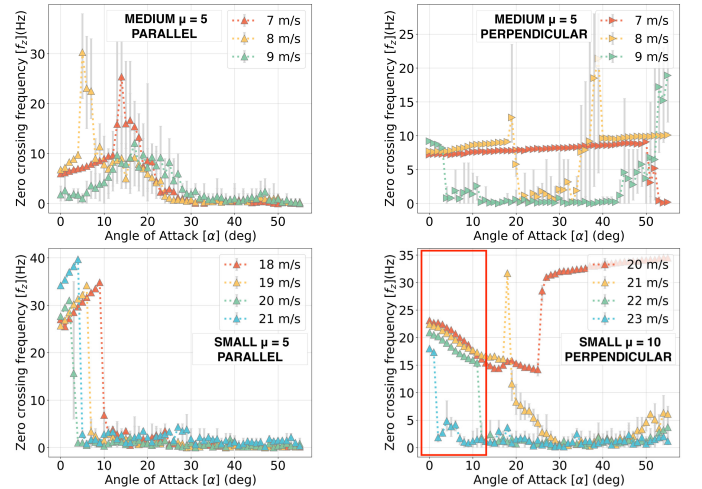
Fig. 9: Evaluation of zero crossing frequency variation for different α, U and flag orientation.

500 ms. f_z is calculated over 500 ms intervals. The wind speed ranges considered directly follows from the energy harvesting performance of each flag across the ranges of U and α. It was found that for both mass ratios, the perpendicular configuration showed a more uniform decaying trend of V_p with α. However, for certain ranges of $\alpha \in [15°, 25°]$ for $\mu=5$ and $\alpha \in [10°, 30°]$ for $\mu=10$, the perpendicular flags showed a peak which could be attributed to the flag being exposed to a cross-flow
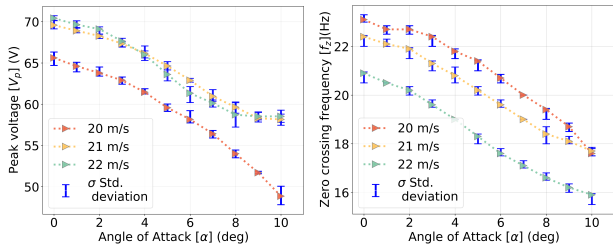
Fig. 10: Repeatability of voltage and frequency measurements indicating robustness of Hermes

Fig. 11: Hermes system block diagram and fabricated sensor.

component that induces flutter. The flags oriented in parallel do not show this phenomenon as expected from their orientation. At $\alpha > 10°$, these flags remain in the bent mode and do not show any significant flapping. The perpendicularly oriented flags are less affected by changing α. All flags show increased sensitivity to changes in α at higher E as expected. The high variability in the observed f_z at $\alpha > 10°$ is due to low amplitude flapping of the flags at these angles.

Fig. 8 confirms that oscillations are not large, and the flags are in deflected mode. Even in that mode, these low amplitude flutter oscillations still created high-frequency components in the flags. The variation in frequency for the small flag in perpendicular configuration shows its potential for carrying information regarding α and U in the range $\alpha \in [0°, 10°]$. From these results, it is evident that only the small flag in the perpendicular configuration shows an invertible relationship between (α, U) and (V_p, f_z). This cements the decision for the use of the small flag in the perpendicular configuration as the sensing element in Hermes. Since each flag has a 10° range for effective AoA sensing, we propose to use a multitude of small flags in order to obtain a higher AoA sensing range of Hermes, as discussed in the next section. Fig. 10 shows the variability of the voltage and frequency measurements for particular AoA and wind speeds. Each AoA and wind speed pair were repeated 30 times. Here it can be seen from the low standard deviation that there is an appreciable degree of repeatability/uniqueness in voltage and frequency measurements for a particular aerodynamic state (α, U). This demonstrates the reliability of Hermes.

V. Design of Hermes

A. System design

Based on the controlled experiments and insights gained from Section III, we carry out the design of the proposed system. The system consists of three functional blocks: piezoelectric flag, energy conditioning, and the microcontroller and sensing.

1) Piezoelectric flag: This block consists of an array of five single poled PVDF piezoelectric films ($L = 30$ mm, $W = 15$ mm and $\mu = 10$) which are used as inverted flags oriented in the perpendicular configuration (direction of flutter in $x - y$ plane). These flags form both the sensing as well as the harvesting element. Each of the flags is mounted at an angle of 10° from the other. Fig. 11 shows the fabricated Hermes sensor with all of the system blocks along with the mechanical mount
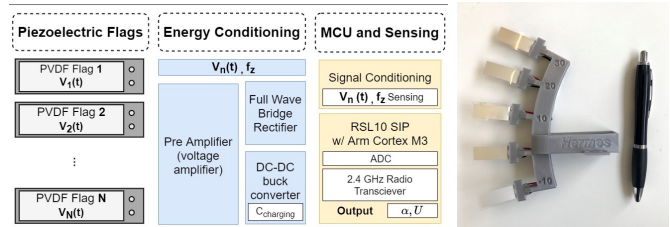
design. The flags are held in place using specially designed rigid clamps that orient the flags at the required mount angle. Each flag, based on the incoming wind direction, will exhibit prominent flapping in a range of $[0, 10]°$ from the central axis of the flag. Together, at least one of these five flags will flutter within a 40° range in wind direction. The generated voltage from each flag is fed to the energy conditioning block for harvesting and sensing.

2) Energy conditioning: The output of each flag, $V_N(t)$, $1 \leq N \leq 5$ is fed to a pre-amplifier, which is used as a voltage amplifier for the piezoelectric films and functions as a buffer between the piezoelectric films and the rest of the circuit. The pre-amplifier output is fed to the signal conditioning circuit before being sampled by the ADC in the microcontroller and to the power harvesting and rectifying circuit for powering the sensor as well. The output of the buck converter is directly used to power the microcontroller.

3) Micro controller and sensing: The signal $V_N(t)$ needs to be conditioned to make it possible for the ADC to sample it. This is done by using a resistive voltage divider circuit for voltage scaling and an ultra low-power OpAmp for inverting the negative swing of the voltage waveform.

We use ON Semiconductors RSL10 System-In-Package (RSL10 SIP) as the microcontroller and radio chip, which contains an integrated onboard antenna, BLE radio SoC and all necessary passive components in a single package. It is ultra-low power and has a highly flexible multi-protocol 2.4GHz radio. The ADC in RSL10 can record voltage between 0 to 2 V, and can sequentially sample 8 channels at a maximum sampling rate of 6.25 kHz with a resolution of 14 bits. Using this microcontroller, the entire sensor design requires $360\,\mu$J to communicate at 6 dBm maximum transmit power. We sample the $V_N(t)$ signal after it is passed through the signal conditioning block for each of the piezoelectric flags at 1 kHz sampling rate for 500 ms. This recorded signal is then fed into the real-time algorithm (discussed in Section V-B) for estimation of α and U. Once that is calculated, the SIP transmits the measured quantities as BLE beacons using one of the three advertising channels. In the current design, the sensor continuously broadcasts sensed data at a rate of 2 Hz in the presence of wind.

The sensor is mounted at the leading edge of the airfoil of the aircraft. Since the sensor faces the incoming wind without a bluff body, wake effects can be ignored if the sensor is mounted sufficiently far away from the fuselage. The volumetric size of the mount and sensors is 27.5 cm^3 and the weight of the flags and sensor PCB without the mount is about 60 g.
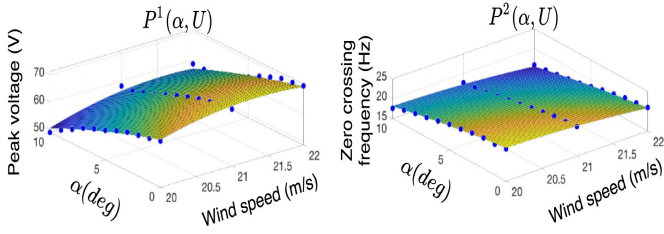
Fig. 12: Surface polynomials for expressing V_{pN} and f_z as functions of α and U.

B. NSR Algorithm for estimating AoA, wind speed

We propose *Nonlinear Surface Regression* (NSR) – an estimation algorithm that uses the generated voltage signals from the piezoelectric flag array to dynamically estimate the AoA and wind speed from the incoming airflow. The algorithm comprises of three stages: i) *Nonlinear surface generation*, ii) *AoA range separation*, and iii) *Iterative nonlinear inversion*. Stage i) is performed once, offline, during calibration, while ii) and iii) are performed online in the respective sequence.

1) Stage 1: Nonlinear surface generation: From the voltage signal $V_N(t)$ of each piezoelectric flag, where $1 \leq N \leq 5$, the peak voltage V_{pN} and zero-crossing frequency f_{zN} have been averaged over $500\,\mathrm{ms}$ of data, generating time-series $V_{pN}(t_k)$ and $f_{zN}(t_k)$ sampled at $0.5\,\mathrm{Hz}$. From Figs. 8 and 9, it can be seen that V_{pN} and f_{zN} exhibit a monotonic trend when $\alpha \in [0,\,10]°$ and $U \in [20,\,22]$ m/s for the small perpendicularly oriented piezoelectric flag. Therefore, using the data points in Fig. 8 and Fig. 9, an empirical nonlinear relation has been derived as $V_{pN} = P^1(\alpha, U)$, $f_{zN} = P^2(\alpha, U)$, where $P^i(\alpha, U) = \sum_{j=0}^{2} \sum_{k=0}^{2} P^i_{j,k} U^j \alpha^k$. The coefficients $P^i_{j,k}$, have been determined using a *robust linear least squares* algorithm, and the corresponding surface polynomials have been shown in Fig. 12. We determine that $\frac{\partial(P^1, P^2)}{\partial(\alpha, U)}$ is full rank within the sensing range of α, U and therefore from the *inverse function theorem*, we deduce that the relation $(V_{pN}, f_{zN}) = \left(P^1(U, \alpha), P^2(U, \alpha) \right)$ is invertible, allowing us to determine α, U from V_{pN}, f_{zN} as long as $0 \leq \alpha \leq 10°$. The inverse relation can be computed by integrating the rows of $\left(\frac{\partial(P^1, P^2)}{\partial(\alpha, U)} \right)^{-1}$ which represent differential 1-forms of the inverse coordinate functions. However, in this paper a numerical inversion approach based on Newton-Raphson method is followed. When applying a numerical technique however, the convergence depends on the largest Eigenvalue of the Jacobian. In particular, the step size has to be small enough, proportional to the inverse of the largest Eigenvalue. Note that since the trend for V_{pN} and f_{zN} is independent of the sign of α, we only obtain $|\alpha|$ when $\alpha < 0$ via surface polynomials.

2) Stage 2: Determining AoA range: From the structure of Hermes (Fig. 1b), notice that when the $\alpha \in [-10°, 30°]$, at least one of the five piezoelectric flags is within an angular separation of $10°$ from the wind velocity vector $\vec{U}$, as illustrated in Fig. 13. Since the nonlinear surface regression is only
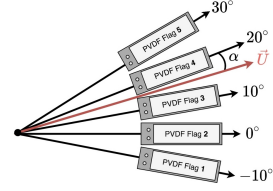
Fig. 13: Schematic of piezoelectric flag array for sensing a wide range of AoA

Algorithm 1: AoA range detection algorithm

Result: Determine:
  1) N such that the Nth piezo makes minimal angle α_N with $\vec{U}$,
  2) $\mathrm{sign}\,(\alpha_N)$

1   Set $N = \min \left(\arg \max_{1 \leq i \leq 5} (V_{pN}) \right)$

2   **if** $1 < N < 5$ **then**
3   **if** $V_{pN+1} < V_{pN-1}$ **then**
4         $\mathrm{sign}\,(\alpha_N) > 0$
5   **else**
6         $\mathrm{sign}\,(\alpha_N) < 0$
7   **else**
8   **if** $N = 5$ **then**
9         $\mathrm{sign}\,(\alpha_N) < 0$
10   **else**
11        $\mathrm{sign}\,(\alpha_N) > 0$
12   **end**

---

applicable when α is within $\pm 10°$, it is necessary to determine the piezoelectric flag which is within this range, and which makes a minimal angle with $\vec{U}$. Further, since the surface regression only gives us the absolute value of the angular separation, it is necessary to determine the sign of the angular separation as well. The above is achieved via Algorithm 1. The algorithm is based on the fact that in the case of the small-size piezo flag in a perpendicular orientation (as seen in the fourth quadrant of Fig. 8), the flag which makes a minimal angle with the wind velocity vector also generates the largest V_p. This is because, as seen in Fig. 13, if one of the piezo flags makes a minimal absolute angle α, then all other piezo flags make an absolute angle which is in the set $\{10i \pm \alpha,\ 1 \leq i \leq 4\}$, and it can be observed that $V_p(\alpha, U) > V_p(10i \pm \alpha, U),\ 1 \leq i \leq 4$.

Stage 3: Iterative nonlinear inversion: Having determined n and $\mathrm{sign}(\alpha_n)$ in the previous step, we now describe an iterative algorithm for determining $|\alpha_N|$, based on Newton-Raphson method. From the full rank condition, there exists an inverse relation $(|\alpha_N|, U) = P^{-1}(V_{pN}, f_z)$, where P^{-1} is computed iteratively via Algorithm 2. Here γ is the step size of the iterations and tol is the error bound. For our implementation we set $tol = 0.01$ and $\gamma = 0.5$. The NSR algorithm was designed such that it has advantages over other data driven methods such as neural networks etc, due to its simplicity, and real-time performance. The dimension of the surface polynomials was minimized to ensure low sensing error and fast convergence. While complex nonlinear inversion algorithms exist, we chose a simple one as the computed

---

Algorithm 2: Iterative nonlinear inversion for AoA, wind speed

---

Result: Determine (α, U) given (V_{pN}, f_{zN})

1 Obtain N and $\text{sign}(\alpha_N)$ from Algorithm 1; Set $[\bar{\alpha}_N, \bar{U}]$ as a nominal point close to the range in which we estimate $|\alpha_N|, U$;

2 Set

$$\begin{bmatrix} \bar{\alpha}_N^+ \\ \bar{U}^+ \end{bmatrix} = \begin{bmatrix} \bar{\alpha}_N \\ \bar{U} \end{bmatrix} - \gamma \left[\frac{\partial(P^1, P^2)}{\partial(\bar{\alpha}_N, \bar{U})} \right]^{-1} \begin{bmatrix} P^1(\bar{\alpha}_N, \bar{U}) - V_{pN} \\ P^2(\bar{\alpha}_N, \bar{U}) - f_{zN} \end{bmatrix},$$

3 if $(\bar{\alpha}_N - \bar{\alpha}_N^+)^2 + (\bar{U} - \bar{U}^+)^2 < tol$ **then**

4 $|\alpha_N| = \bar{\alpha}_N^+, U = \bar{U}^+$, go to step 7

5 else

6   Set $\bar{\alpha}_N = \bar{\alpha}_N^+, \bar{U} = \bar{U}^+$, go to step 2

7 AoA: $\alpha = 10(N - 2) + |\alpha_N|\text{sign}(\alpha_N)$.
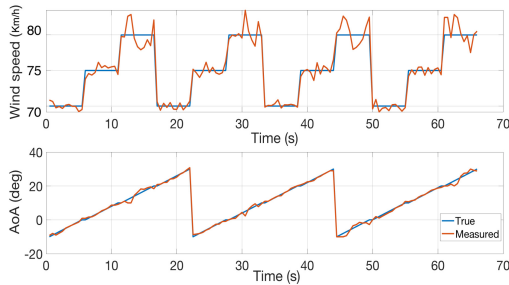
(a) Comparison between actual and estimated wind speed and AoA.
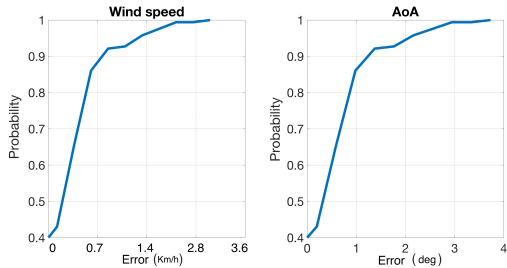
(b) CDF of error in U, α corresponding to Fig. 14a

Fig. 14: Sensing performance of Hermes

relations were sufficiently tractable. Indeed the sensing performance can be further improved by augmenting NSR with filtering methods such as extended Kalman or nonlinear filters by using NSR as the instantaneous output of the filtering equations which use past measurements to improve the sensing accuracy. This step is planned as a future extension.

VI. EVALUATION RESULTS AND DISCUSSION

We study the performance of Hermes in the wind tunnel by varying $\alpha \in [-10°, 30°]$ and $U \in [70, 80]$ km/h. Fig. 14a shows the comparison between actual and estimated values of α and U. It can be seen that the accuracy of α is significant, substantiating the high performance of Hermes. In Fig. 14b, we also plot the CDF of estimation errors. While the estimation error of U is below 0.7 km/h with 90% probability, the error of α is within 1.2° with 90% probability and within 2° with 95% probability. For the chosen averaging interval (for V_p and f_z) and the parameters of the Newton algorithm,
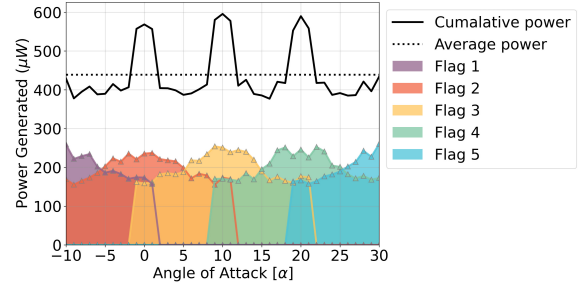
Fig. 15: Energy harvested by the sensor over entire operational range by different flags.
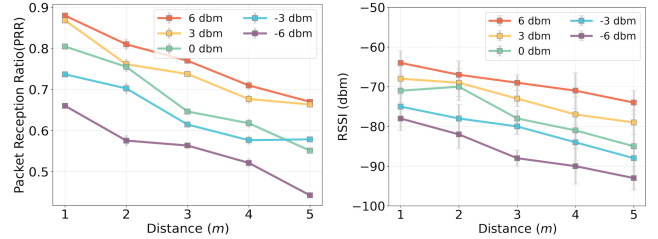
Fig. 16: Packet reception ratio (PRR) and RSSI of for varying distance and transmission power.

the sensing rate is 2 Hz. Sensing accuracy can be improved by varying the tolerance, error bound, averaging interval and polynomial degree.

Fig. 15 shows the energy harvested by Hermes over the entire range of α. It can be seen that Hermes can harvest at least 377 μW and a mean of 440 μW over the considered range of α. Note that energy harvested from multiple films can be utilized simultaneously, unlike AoA which is drawn from only one film. This results in a power density of 2.16 mW/cm^3 per film.This power is sufficient for transmitting the sensed value at 2 Hz at low transmission power (0 dBm and lower) and at 1 Hz for max transmission power (6 dBm). The sensor harvests enough energy to power a wide band radio chip while also sensing other parameters like temperature and humidity, which may be used to assess the airspeed from dynamic pressure.

We vary the distance between Hermes and BLE receiver from 1 m to 5 m and transmission power from 6 dBm to -6 dBm. Fig. 16 shows the variation of Packet Reception Ratio (PRR) and RSSI measured throughout 500 s. It can be seen that Hermes can achieve a maximum PRR of 89% at transmission power of 3 dBm and 6 dBm. This shows that reasonably reliable communication is achieved.

Hermes measures a total span of 4.67 cm with a volume of 27.5 cm^3 and weighs 135 g. Table II compares Hermes with commercially available sensors. Since pitot tubes are static sensing systems, they have a tendency for blockage and accumulation of water / ice / snow causing pressure transducers to malfunction. Our system does not have cavities, and is also less prone to clogging due to continuous. Further, the piezoelectric element of the PVDF films is isolated from the external environment by a laminate layer of Mylar rendering it resistant to dust.

In our current experiments, the sensing range of wind speed is limited, due to the limited flutter range. However, as shown in Fig. 5 it can be seen that the flutter range can be drastically

TABLE II: Comparison with state-of-the-art sensors

	UTC Aerospace [11]	Aeroprobe [12]	Hermes
Form factor	10.2 cm, 907.2 g	>20 cm, >350g	4.67 cm, 134.2 g
Type	AoA	AoA, Wind speed	AoA, Wind speed
Operational Power	100W	30 W	440* μW
Sensing Accuracy	>1.5°	1°, 1 m/s	1.2°(90%) 0.2 m/s (90%)

varied by changing the geometric characteristics of the peizo film. Currently we have used commercial films which limited our sensing range, however this can be significantly improved by customizing the morphology and geometric characteristics of the films. Future work that has been planned involves custom designing the geometry of the films in order to optimize sensing range. We also plan to use piezo films of different aspect ratios for different ranges as well.

VII. CONCLUSIONS

We proposed a novel sensor - Hermes, which measured the Angle of Attack (AoA) and wind speed simultaneously with appreciable accuracy. Our prototype comprised a compact array of piezoelectric films which generate voltage signals due to the aerodynamic flutter in the wind flow. Hermes is self-powered by harnessing the flutter to measure AoA and wind speed. We built a small form factor, proof of concept sensor that is batteryless, self-powered, and wireless. We proposed a new real-time algorithm to process the piezoelectric signals, enabling simultaneous measurement of AoA and wind speed. Further, the flutter-based mechanical design also enabled simultaneous maximization of sensing performance and energy harvesting capability, without sacrificing either harvesting efficiency or accuracy. Hermes was evaluated through extensive wind tunnel experiments. We estimated the AoA and wind speed with an accuracy of 1.2° and 0.7 km/h with 90% probability, respectively. Hermes can send two measurements every second when harvested energy is maximum, which is more than sufficient for most of the applications. The inexpensive, compact, and wireless design of Hermes enables a wide range of applications for piloted and unmanned flight systems, as well as other applications such as automating the wind farms for maximum harvesting, navigation of ships, trains, and smart grids. Some videos of wind tunnel experiments can be accessed in the *youtube link* given in the following reference **here [23]**. The current prototype was made with commercial off the shelf piezoelectric strips with fixed dimensions. Further efforts are underway to custom print the strips to vary the aspect ratio and bending stiffness to increase the sensing range and rate.

VIII. ACKNOWLEDGEMENT

REFERENCES

[1] A. Lambregts, G. Nesemeier, R. Newman, and J. Wilborn, "Airplane upsets: Old problem, new issues," in *AIAA Modeling and Simulation Technologies Conference and Exhibit*, 2008, p. 6867.

[2] F. Culick, "The wright brothers: first aeronautical engineers and test pilots," *AIAA journal*, vol. 41, no. 6, pp. 985–1006, 2003.

[3] S. Imai, E. Blasch, A. Galli, W. Zhu, F. Lee, and C. A. Varela, "Airplane flight safety using error-tolerant data stream processing," *IEEE Aerospace and Electronic Systems Magazine*, vol. 32, no. 4, pp. 4–17, 2017.

[4] B.E.A. (2020) Interim report on the accident on 1st june 2009 to the airbus a330-203 registered f-gzcp operated by air france flight af 447 rio de janeiro – paris. Accessed: 2020-8-21.

[5] I. N. T. S. C. (NTSC). (2018) Preliminary aircraft accident investigation report: Lion air flight 610. Accessed: 2020-8-21. [Online]. Available: http://knkt.dephub.go.id/knkt/ntscaviation/baru/pre/2018/2018%20-%20035%20-%20PK-LQP%20Preliminary%20Report.pdf

[6] Boeing. (2020) Aero 12: Angle of attack story. Accessed: 2020-8-21. [Online]. Available: http://www.boeing.com/commercial/aeromagazine/aero_12/attack_story.html

[7] Mi-Hyun Park, Sung-Su Kim, Chang-Kyung Ryoo, Keeyoung Choi, and Choonbae Park, "Development of alpha sensor for unmanned aerial systems," in *2008 SICE Annual Conference*, 2008, pp. 2131–2134.

[8] P. Pačes, K. Draxler, T. Čenský, V. Hanzal, and O. Vaško, "A combined angle of attack and angle of sideslip smart probe with twin differential sensor modules and doubled output signal," in *SENSORS, 2010 IEEE*, 2010, pp. 284–289.

[9] T. A. Johansen, A. Cristofaro, K. Sørensen, J. M. Hansen, and T. I. Fossen, "On estimation of wind velocity, angle-of-attack and sideslip angle of small uavs using standard sensors," in *2015 International Conference on Unmanned Aircraft Systems (ICUAS)*, 2015, pp. 510–519.

[10] M. Oosterom and R. Babuska, "Virtual sensor for the angle-of-attack signal in small commercial aircraft," in *2006 IEEE International Conference on Fuzzy Systems*, 2006, pp. 1396–1403.

[11] U. A. Rosemount. (2020) Model 0861h. Accessed: 2020-8-21. [Online]. Available: http://goodrich.com/cap/systems/Pages/SIS-document-library.aspx

[12] Aeroprobe. (2020) Air data probe. Accessed: 2020-8-21. [Online]. Available: http://www.aeroprobe.com/air-data-probe/

[13] Y. Tan and S. Panda, "A novel piezoelectric based wind energy harvester for low-power autonomous wind speed sensor," in *IECON 2007-33rd Annual Conference of the IEEE Industrial Electronics Society*. IEEE, 2007, pp. 2175–2180.

[14] J. E. d. P. Braquehais and A. A. Lisboa de Souza, "Energy-autonomous wind speed smart sensor," in *2014 IEEE International Instrumentation and Measurement Technology Conference (I2MTC) Proceedings*, 2014, pp. 931–935.

[15] M. J. Shelley and J. Zhang, "Flapping and bending bodies interacting with fluid flows," *Annual Review of Fluid Mechanics*, vol. 43, pp. 449–465, 2011.

[16] J. McCarthy, S. Watkins, A. Deivasigamani, and S. John, "Fluttering energy harvesters in the wind: A review," *Journal of Sound and Vibration*, vol. 361, pp. 355–377, 2016.

[17] D. Kim, J. Cossé, C. H. Cerdeira, and M. Gharib, "Flapping dynamics of an inverted flag," *Journal of Fluid Mechanics*, vol. 736, 2013.

[18] S. Alben and M. J. Shelley, "Flapping states of a flag in an inviscid fluid: bistability and the transition to chaos," *Physical review letters*, vol. 100, no. 7, p. 074301, 2008.

[19] B. S. Connell and D. K. Yue, "Flapping dynamics of a flag in a uniform stream," *Journal of fluid mechanics*, vol. 581, p. 33, 2007.

[20] S. Michelin, S. G. Llewellyn Smith, and B. J. Glover, "Vortex shedding model of a flapping flag," *Journal of Fluid Mechanics*, vol. 617, no. 1, pp. 1–10, 2008.

[21] J. Ryu, S. G. Park, B. Kim, and H. J. Sung, "Flapping dynamics of an inverted flag in a uniform flow," *Journal of Fluids and Structures*, vol. 57, pp. 159–169, 2015.

[22] S. Orrego, K. Shoele, A. Ruas, K. Doran, B. Caggiano, R. Mittal, and S. H. Kang, "Harvesting ambient wind energy with an inverted piezoelectric flag," *Applied energy*, vol. 194, pp. 212–222, 2017.

[23] Hermes. (2020) Hermes flutter video demonstration. Created: 2020-8-21. [Online]. Available: https://youtube.com/playlist?list=PLMRGaMAoy1AHBoIldlAZ9AJaeamNun_Bm

[24] *Piezo Film Product Guide and Price List*, Measurement Specialties, Inc., 10 2008, rev. 1.